



PCCP

Unlocking the key to persistent luminescence with X-ray absorption spectroscopy: A local structure investigation of Cr-substituted spinel-type phosphors

| | |
|-------------------------------|---|
| Journal: | <i>Physical Chemistry Chemical Physics</i> |
| Manuscript ID | CP-ART-05-2019-002655.R3 |
| Article Type: | Paper |
| Date Submitted by the Author: | 15-Aug-2019 |
| Complete List of Authors: | Finley, Erin; University of Houston, Gaultois, Michael; University of Liverpool, Department of Chemistry Brgoch, Jakoah; University of Houston, Chemistry |
| | |

SCHOLARONE™
Manuscripts

Unlocking the key to persistent luminescence with X-ray absorption spectroscopy: A local structure investigation of Cr-substituted spinel-type phosphors

Erin Finley¹, Michael W Gaultois², Jakoah Brgoch^{1*}

¹*Department of Chemistry, University of Houston, Houston, TX 77204*

²*Leverhulme Research Center for Functional Material Design, Materials Innovation Factory, Department of Chemistry, University of Liverpool, Liverpool L7 3NY, United Kingdom*

Abstract

Developing new persistent luminescent phosphors, a unique class of inorganic materials that can produce a visible light emission lasting minutes to hours requires improving our understanding of their fundamental structure-property relationships. Research has shown that one of the most critical components governing persistent luminescence is the existence of lattice defects in a material. Specifically, vacancies and anti-site defects that coincide with substitution of the luminescent center, e.g., Eu^{2+} or Cr^{3+} , are generally considered essential to generate the ultra-long luminescent lifetimes. This research solidifies the connection between defects and the remarkable optical properties. The persistent luminescent compound $\text{Zn}(\text{Ga}_{1-x}\text{Al}_x)_2\text{O}_4$ ($x = 0 - 1$), which adopts a spinel-type structure, is investigated by examining the X-ray absorption near-edge structure (XANES) and extended X-ray absorption fine-structure (EXAFS) at the Cr *K* and Zn *K* edges. This investigation reveals a structural distortion of the octahedrally coordinated main group metal site concurrent with increasing Al^{3+} content. Moreover, these results suggest there is a dependence between the local crystallographic distortions, the presence of defects, and a material's persistent luminescence. In combination, this work provides an avenue to understand the connection between the structure-defect-property relationships that govern the properties of many functional inorganic materials.

1. Introduction

Persistent luminescence is a phenomenon observed in crystalline inorganic solids where the presence of a luminescent center, *e.g.*, Cr³⁺ or Eu²⁺, can generate a visible light emission for minutes to hours after the termination of an excitation source.¹ Due to the extraordinarily long luminescent lifetimes of these materials, a wide range of applications has been developed including emergency signage,² medical diagnostics,³⁻⁷ and novelty items such as wristwatch dials or toys. Their diverse functionality has also driven the discovery of novel persistent luminescent phosphors with a range of emission colors and lifetimes, chemical compositions, and structure types. The most notable materials investigated today include a green-emitting SrAl₂O₄:Eu²⁺,Dy³⁺, a blue-emitting Sr₂MgSi₂O₇:Eu²⁺,Dy³⁺, an orange-emitting Ca₂Si₅N₈:Eu²⁺,Tm³⁺, and a near IR-emitting ZnGa₂O₄:Cr³⁺ among others.⁸⁻¹⁰

The mechanism that drives persistent luminescence is widely agreed to include an electron from the luminescent center being photoionized into the conduction band with continued excitation.¹¹⁻¹⁵ This electron is then trapped by a “trap state,” which stems from a defect within the crystal structure or the presence of 5*d*-orbitals from a co-dopant such as Dy³⁺.¹²⁻¹⁵ The application of additional energy (usually thermal) to the material causes the electrons held in the trap states to be slowly released, leading to significantly longer than expected luminescent lifetimes. Research into this mechanism has comprised of work on understanding the relationship between co-dopants and trap states in an attempt to extend the persistent luminescence further or improve emission intensity.^{11, 16, 17} Increasingly, multiple reports suggest lattice defects (anion vacancies or anti-site defects) are essential for the persistent luminescence mechanism.¹⁸⁻²¹ For example, first-principle calculations revealed anion vacancies were responsible for the observed emission

lifetimes in $\text{SrAl}_2\text{O}_4:\text{Eu}^{2+}$ and $\text{CaAl}_2\text{O}_4:\text{Eu}^{2+},\text{Nd}^{3+}$ whereas anti-site (Zn/Ga) defects were the reason for the long luminescence lifetimes in $\text{ZnGa}_2\text{O}_4:\text{Cr}^{3+}$.¹⁸⁻²⁰

Experimental investigations have also helped establish the relationship between defects and optical properties. In one study, the local structure of Eu^{2+} was analyzed using a combination of synchrotron X-ray absorption spectroscopy (XAS)^{22, 23} and electron paramagnetic resonance spectroscopy (EPR)²⁴ to show that oxygen vacancies contributed to the trapping of electrons in $\text{Sr}_2\text{MgSi}_2\text{O}_7:\text{Eu}^{2+},\text{Dy}^{3+}$. Moreover, ^{71}Ga solid-state NMR of $\text{ZnGa}_2\text{O}_4:\text{Cr}^{3+}$ confirmed anti-site defects were present and with EPR showing the resulting trap states lie next to the first cationic neighbor with respect to Cr^{3+} .²⁵
²⁶ These techniques have each provided strong evidence supporting the need for defects to induce persistent luminescence, but they are not able to uncover explicit structural details connecting any changes in the local coordination environments of these materials that may result due to the presence of defects.

This interest in understanding how the local structure around the luminescent center influences persistent luminescence has been partially investigated in the Cr^{3+} substituted spinel-type phosphors. The most likely origin stems from the presence of anti-site defects that influence the Cr^{3+} polyhedron in the structure.^{9, 26, 27} Fortunately, these spinel structures provide an attractive platform to study the implications of structural defects around Cr^{3+} because the defects can be studied as a function of chemical composition.²⁵
^{28, 29} The family of normal spinel-type structures, AB_2O_4 (A = divalent cation and B = trivalent cation) form in a cubic closed packed structure, space group $Fd\bar{3}m$ (no. 227), with eight tetrahedral A -sites and sixteen octahedral B -sites. In comparison, inverse spinel-type structures have eight of the trivalent B atoms occupying the eight A -sites and the divalent A atoms evenly distributed with the remaining eight B atoms over the sixteen B -

sites. Within this family of spinel-type structures, persistent luminescence has been comprehensively investigated for three compounds: $\text{ZnGa}_2\text{O}_4:\text{Cr}^{3+}$, $\text{ZnAl}_2\text{O}_4:\text{Cr}^{3+}$, and $\text{MgGa}_2\text{O}_4:\text{Cr}^{3+}$.^{26-28, 30-33} The collection of these findings conclusively proved $\text{ZnGa}_2\text{O}_4:\text{Cr}^{3+}$ exhibits the most extended reported lifetime lasting for ≥ 5 h, $\text{MgGa}_2\text{O}_4:\text{Cr}^{3+}$ shows a lifetime of ≤ 15 min, and $\text{ZnAl}_2\text{O}_4:\text{Cr}^{3+}$ does not have a measurable persistent luminescent lifetime.^{28, 30-32}

Most importantly, this work also found that $\text{ZnAl}_2\text{O}_4:\text{Cr}^{3+}$ crystallizes as a nearly perfect normal spinel with Zn almost exclusively occupying the *A* sites and Al occupying the *B* sites. This is different from $\text{ZnGa}_2\text{O}_4:\text{Cr}^{3+}$, which has been suggested to contain $\sim 3\%$ Zn/Ga inversion, *i.e.*, anti-site defects.²⁵ $\text{MgGa}_2\text{O}_4:\text{Cr}^{3+}$ shows an entirely different behavior with $\sim 44\%$ Mg/Ga inversion.^{31, 32} There is an apparent connection between the concentration of the anti-site defects and the luminescent lifetimes; therefore, the relationship between persistent luminescence and anti-site defects should be probed. Prior research using photon emission and thermoluminescence spectroscopies to study $\text{Zn}(\text{Ga}_{1-x}\text{Al}_x)_2\text{O}_4:\text{Cr}^{3+}$ showed there is a dependence on the number of lattice defects stemming from the different Al content as a function of x .²¹ Additionally, a study of $(\text{Zn}_{1-x}\text{Mg}_x)\text{Ga}_2\text{O}_4:\text{Cr}^{3+}$ using EPR and XAS, of Cr^{3+} indicated a correlation between anti-site defects and local structure by identifying a decrease in bond length between Cr–O with an increasing number of defects.²⁸

The substitution of Cr^{3+} in these spinel-type crystal structures not only induces defects leading to the formation of trap states, but it also causes the normally octahedrally coordinated *B*-site to undergo a trigonal distortion, reducing the point group symmetry from O_h to D_{3d} .³⁴ This distortion can be observed in the photoemission of $\text{ZnGa}_2\text{O}_4:\text{Cr}^{3+}$ and $\text{ZnAl}_2\text{O}_4:\text{Cr}^{3+}$; where there is an observed ${}^2E_g \rightarrow {}^4A_{2g}$ photon emission, which is formally

spin-forbidden in an exact, *i.e.*, undistorted, O_h symmetry. Detailed analysis of this photon emission at 77 K revealed a splitting of the emission peak into two distinct peaks confirming a lowering of the symmetry from O_h (${}^2E_g \rightarrow {}^4A_{2g}$) to D_{3d} ($E_g \rightarrow {}^4A_{2g}$ and $2A_g \rightarrow {}^4A_{2g}$), where the gallate ($\approx 40 \text{ cm}^{-1}$) had a more significant splitting of the E_g and $2A_g$ versus the aluminate ($\approx 6 \text{ cm}^{-1}$).³⁴⁻³⁶

An examination of the relationship between the trigonal distortions of Cr^{3+} in $\text{ZnGa}_2\text{O}_4:\text{Cr}^{3+}$, $\text{ZnAl}_2\text{O}_4:\text{Cr}^{3+}$, and $\text{MgGa}_2\text{O}_4:\text{Cr}^{3+}$ and anti-site defects were subsequently conducted using EPR.³² This study showed that strain broadening, which is an indication of anti-site defects, increased with defect concentration following $\text{MgGa}_2\text{O}_4:\text{Cr}^{3+} > \text{ZnGa}_2\text{O}_4:\text{Cr}^{3+} > \text{ZnAl}_2\text{O}_4:\text{Cr}^{3+}$. This result provided further evidence consistent with the known inversion of these materials and the observed splitting of the E_g and $2A_g$ states.^{32, 35} The EPR study also showed the zero-field splitting of the 4A_2 ground state with $\text{ZnAl}_2\text{O}_4:\text{Cr}^{3+} > \text{MgGa}_2\text{O}_4:\text{Cr}^{3+} > \text{ZnGa}_2\text{O}_4:\text{Cr}^{3+}$ suggesting a decreasing trigonal distortion on the C_3 axis.^{32, 35} Intriguingly, the zero-field splitting trend corresponds to the loss of long luminescent lifetimes reported with this family of spinel-type structures, such that as zero-field splitting increases there is a decrease in lifetime.^{26-28, 30-32} These results imply that the relationship between the C_3 axial distortion of Cr^{3+} and anti-site defects are linked to persistent luminescence. However, in all of these studies, the relationship between the defects and the changes in the (local) structure around the actual luminescent center is only indirectly probed.

In the research presented here, the local structure surrounding the Cr^{3+} ion is explicitly investigated across the solid solution $\text{Zn}(\text{Ga}_{1-x}\text{Al}_x)_2\text{O}_4:\text{Cr}^{3+}$ ($x = 0 - 1$) using XAS to investigate the X-ray absorption near edge structure (XANES) and extended X-ray absorption fine structure (EXAFS) to determine the local structure. The previously reported

optical properties, with respect to persistent luminescence of this solid solution, were measured by charging each sample across all values of x with a 254 nm light source.²¹ Using an excitation source that is greater than the measured optical band populates all available traps states, i.e., lattice defects; however, only those trap states >0.4 eV and <1.0 eV can be considered as participating in the persistent luminescent mechanism.^{14, 21, 37} Nevertheless, the results revealed there was a significant quenching of the long luminescent lifetime, in the visible region of the electromagnetic spectrum, with increasing aluminum content from $x = 0 - 0.50$, with the persistent luminescence completely quenched at $x = 0.75$.²¹ The loss of persistent luminescence in the visible region in this series was indirectly attributed to an increase in the number of lattice defects that became shallower as Al^{3+} content increased up to $x = 0.50$.²¹ This important finding is now bolstered by the present report, which provides direct crystallographic evidence of local distortions and point defects in these spinel-type crystal structures. These results make possible a stronger understanding of the structure-defect-property relationship that will be critical for developing new persistent luminescence phosphors.

2 Experimental

2.1 Sample Preparation and Characterization

Polycrystalline samples with the nominal compositions $\text{Zn}(\text{Ga}_{1-x}\text{Al}_x)_{1.995}\text{Cr}_{0.005}\text{O}_4:\text{Cr}^{3+}$ ($x = 0, 0.25, 0.50, 0.75, 1$) were prepared *via* high-temperature solid-state synthesis. The starting materials were weighed out in stoichiometric ratios using the following reagents: ZnO (Alfa Aesar 99.9%), Ga_2O_3 (Alfa Aesar 99.95%), Al_2O_3 (Alfa Aesar 99%), Cr_2O_3 (Alfa Aesar 99%). Additionally, 4 wt% boric acid (Sigma Aldrich 99.98%) was added as a flux. These powders were first mixed using a shaker mill (Spex 8000M) in a polystyrene vial

with 9.5 mm methacrylate balls as grinding media for 45 min and then pressed into 8 mm pellets. The pellets were heated in air for 10 h at 1300°C with heating and cooling rates of 3°C/min. The products were subsequently ground into fine powders using an agate mortar and pestle for characterization.²¹ As stated in our previous publication the powders were confirmed by X-ray diffraction was performed using a PanAnalytical X'Pert powder diffractometer equipped with Cu K α radiation (1.54183 Å) to evaluate the identity and purity of the product (Figure 1).

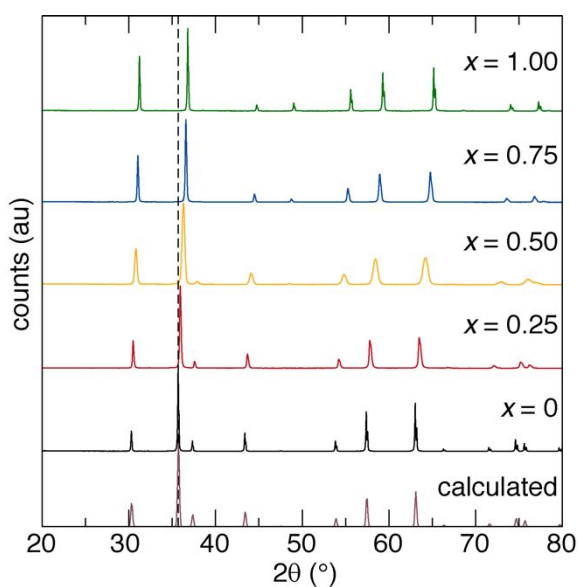


Figure 1. Powder X-ray diffraction of $\text{Zn}(\text{Ga}_{1-x}\text{Al}_x)_2\text{O}_4:\text{Cr}^{3+}$ ($x = 0 - 1$). The whole solid solution forms in the space group $Fd\bar{3}m$ (no. 227), and is well-modeled by the calculated pattern.³⁸ The increasing substitution of Al^{3+} for Ga^{3+} is confirmed by the shift of reflections to higher angle, as expected from a decrease in unit cell volume.

All peaks correspond to the intended phase, indicating there are no impurities within the detection limit. The powders were then sent to Advanced Photon Source at Argon National Laboratory 11-BM for high-resolution synchrotron radiation.²¹ The results were analyzed via Rietveld refinement and were confirmed to be a single phase for each composition and

can be seen in the supporting information of reference 21.²¹ The corresponding site occupancies are presented in Table 1 and the additional crystallographic data can be found in the supporting information of reference 21.²¹ The interatomic distances determined by Rietveld refinement against the obtained diffractograms are presented in Table S1.²¹ It should be noted that due to the low concentration of Cr³⁺ it could not be refined.

Table 1. Site occupancy of Zn(Ga_{1-x}Al_x)₂O₄:Cr³⁺ ($x = 0 - 1$), determined by Rietveld refinement.²¹

| Atom | Wyck. site | Occup. |
|----------------------------------|------------|----------|
| (a) $x = 0$ | | |
| Zn | 8a | 1 |
| Ga | 16d | 1 |
| O | 32e | 1 |
| (b) $x = 0.25$ | | |
| Zn | 8a | 1 |
| Ga | 16d | 0.740(1) |
| Al | 16d | 0.260(1) |
| O | 32e | 1 |
| (c) $x = 0.50$ | | |
| Zn | 8a | 1 |
| Ga | 16d | 0.497(1) |
| Al | 16d | 0.503(1) |
| O | 32e | 1 |
| (d) $x = 0.75$ | | |
| Zn | 8a | 1 |
| Ga | 16d | 0.238(1) |
| Al | 16d | 0.762(1) |
| O | 32e | 1 |
| (e) $x = 1$ | | |
| Zn | 8a | 1 |
| Al | 16d | 1 |
| O | 32e | 1 |

2.2 Density Functional Theory Calculations

Structure optimization for $\text{Zn}(\text{Ga}_{1-x}\text{Al}_x)_2\text{O}_4$ ($x = 0, 0.25, 0.50, 0.75, 1$) was conducted using the Vienna *ab initio* Simulation Package (VASP).³⁹ All calculations employed a plane-wave basis set with projector augmented wave (PAW) potentials.^{40, 41} The atomic positions and unit cell volumes were relaxed within the Generalized Gradient Approximation (GGA), and the exchange and correlation described using the Perdew-Burke-Ernzerhof (PBE) functional.⁴² Total energy calculations used a plane-wave cutoff energy of 500 eV and a $2 \times 2 \times 2$ Γ -centered Monkhorst-Pack k -point mesh with convergence criteria of 1×10^{-8} eV for the electronic relaxation and 1×10^{-6} eV for the structural relaxation. All of the crystal structures were visualized using VESTA.⁴³

2.3 X-ray Absorption Spectroscopy

XANES and EXAFS measurements were carried out in conjunction with the Materials Research Collaborative Access Team (MRCAT) at the Advanced Photon Source, Argonne National Laboratory on the 10-BM beamline.^{44, 45} For this analysis, the samples were finely ground and sieved to a uniform size of -325 mesh (Cole Palmer) and then spread thinly over Kapton™ tape. Spectra were collected at the Cr K edge (5989 eV) in fluorescence mode between 5000 eV and 7000 eV, and at the Zn K edge (9659 eV) in transmission mode between 9410 eV and 9659 eV. Data analysis was conducted using the Athena and Artemis software packages.⁴⁶ In each of the compositions, the independent variables fit were N (degeneracy of the absorbing atom), r (interatomic distance of the atomic neighbors), Δr (the difference between r_{DFT} where r stems from the DFT-optimized structure and r), and σ^2 (the Debye-Waller factor).

3 Results and Discussion

3.1 XANES Spectra of the Cr K Edge

X-ray absorption spectroscopy (XAS) was conducted using the solid solution $\text{Zn}(\text{Ga}_{1-x}\text{Al}_x)_2\text{O}_4:\text{Cr}^{3+}$ ($x = 0 - 1$) to investigate the local structural environment of Cr^{3+} . Owing to the low concentrations of Cr^{3+} substitution in this crystal structure, refining the specific crystallographic details surrounding the luminescent cation is not easily done using conventional, average structure methods like powder X-ray diffraction. Thus, XAS is a valuable tool for determining structural properties in persistent luminescent materials because these are element-specific measurements.⁴⁷ The X-ray absorption spectrum of a particular absorption edge is often divided into two spectral regions, with distinct features; first, the XANES region, provides information about coordination geometry, orbital mixing, and oxidation state, whereas the second, EXAFS region, provides details about interatomic distances, site occupancies, and coordination environment.⁴⁶⁻⁴⁸

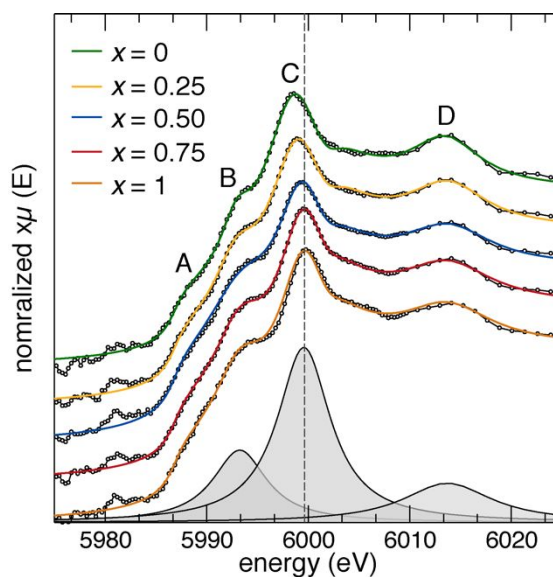


Figure 2. Cr K edge XANES for $\text{Zn}(\text{Ga}_{1-x}\text{Al}_x)_2\text{O}_4:\text{Cr}^{3+}$ ($x = 0 - 1$). The four prominent features: A-B is the $1s \rightarrow 3d$ transition, C is $1s$ -

to-continuum, and D is a scattering peak resulting from the crystal structure (rather than the electronic structure), Lorentzian peaks fit to the data are grey. The dashed line is a guide for the eye to show the shift in the energy of peak C.

In this work, the XANES was collected for the Cr *K* edge in $\text{Zn}(\text{Ga}_{1-x}\text{Al}_x)_2\text{O}_4:\text{Cr}^{3+}$ ($x = 0 - 1$), and is shown in Figure 2. In the pre-edge range, ≤ 5989 eV, there are no intense peaks indicating chromium exists primarily in its 3+ oxidation state.^{49, 50} Further analysis shows there are four prominent features in the XANES data, labeled A, B, C, and D. First are the A (absorption edge at 5989 eV) and B features, which represent the $1s \rightarrow 3d$ photoelectronic transition of Cr^{3+} .⁵¹ Next, the C feature is identified as the electronic transition of an electron from the 1s orbital to continuum states. The C feature shows a shift to higher energy (eV) with increasing Al^{3+} concentration, which is consistent with an increase in the optical bandgap as Al^{3+} increases.^{21, 52, 53} Finally, the D feature is a scattering peak resulting from the constructive interference of emitted photoelectrons and is thus most strongly influenced by the crystal structure, rather than the electronic structure.³³

To gain qualitative insight into how these features change with varying composition, the B, C, and D features were fit using Lorentzian functions, resulting in three distinct peaks (Table 2). The A feature was fit using an arctan step function to model the absorption edge and was set to 5989 eV for all x values. Attempts were made to perform fits with multiple arctan functions, but only models with a single arctan step converged to stable fits; the use of a single arctan step is appropriate in this model because only one species of Cr is present in each composition.

Table 2. XANES peak fitting results for $\text{Zn}(\text{Ga}_{1-x}\text{Al}_x)_2\text{O}_4:\text{Cr}^{3+}$ ($x = 0 - 1$)

| | Centroid (eV) | Height (E) | Width (E) |
|-------|---------------|------------|-----------|
| (a) B | | | |

| | | | |
|-------|------------|---------|--------|
| 0 | 5993(1) | 1.3(3) | 3.7(3) |
| 0.25 | 5993(4) | 2(1) | 5.3(3) |
| 0.50 | 5993(5) | 5(4) | 8.5(3) |
| 0.75 | 5993(1) | 3.6(7) | 6.5(2) |
| 1 | 5993.4(8) | 4.0(5) | 6.7(2) |
| (b) C | | | |
| 0 | 5998.7(1) | 11.1(3) | 7.5(3) |
| 0.25 | 5998.99(9) | 10(1) | 7.3(6) |
| 0.50 | 5999.4(1) | 8(4) | 6.5(7) |
| 0.75 | 5999.58(9) | 8.6(7) | 6.4(1) |
| 1 | 5999.8(1) | 8.2(5) | 6.1(1) |
| (c) D | | | |
| 0 | 6013.5(4) | 3.1(2) | 8.4(8) |
| 0.25 | 6013.8(4) | 3.0(2) | 9.1(9) |
| 0.50 | 6013.8(5) | 3.0(3) | 10(1) |
| 0.75 | 6013.7(4) | 3.2(2) | 11(1) |
| 1 | 6013.8(5) | 3.1(2) | 11(6) |

The energy, intensity, and width of each peak are essential and reveal different aspects of the electronic and crystal structure. First, when examining the peak energy, Table 1 establishes that peaks B and D have a constant energy centroid across the whole range of x , whereas peak C shifts to higher energy with increasing Al^{3+} concentration. The shift in energy by the C peak is a result of the increased electronegativity of Al^{3+} ions compared to Ga^{3+} ions.⁵¹

Second, the intensity of features is also essential, as they are influenced by changes in occupancy of valence orbitals. With increasing Al^{3+} concentration, the intensity of peak D remains unchanged, the intensity of peak B increases, and the intensity of peak C decreases. The increase in the intensity of peak B with increasing Al^{3+} content is due to the increasing presence of the lower energy Cr $3p$ -orbitals that stems from the shifting of the energy of the C peak.⁵¹ The decrease in the intensity in peak C is attributed to a decrease in the number of unoccupied orbitals above the Fermi level due to chemical substitution.⁵¹

Third, the peak widths in XANES have been ascribed to distortions in the $[\text{CrO}_6]$ octahedron, where a broader peak is indicative of more anti-site defects.^{28, 33} From these data, it is evident that peak B broadens as x increases to 0.50 and then narrows going from $x = 0.75$ to $x = 1$. These observations are consistent with an increase in the number of lattice defects that were also observed in a prior thermoluminescence study.²¹ Alternatively, peak C narrows and peak D broadens with increasing Al^{3+} content; these changes are likely due to a change in the atomic interactions between Cr^{3+} and its neighboring atoms with varying x . This is also consistent with a previous report of $\text{ZnGa}_2\text{O}_4:\text{Cr}^{3+}$ and $\text{ZnAl}_2\text{O}_4:\text{Cr}^{3+}$, which found similar changes in XANES peak width and intensity and ascribed the changes to shifts in the Cr–O bond lengths.³³ However, to unambiguously support these claims, it is essential to investigate the Cr^{3+} local structure by examining the EXAFS region and extracting a more precise coordination environment around Cr^{3+} presented below.

3.2 EXAFS Spectra of Cr K Edge

To comprehensively explore how local symmetry distortions observed in the XANES spectra are changing as a function of x , the EXAFS across the $\text{Zn}(\text{Ga}_{1-x}\text{Al}_x)_2\text{O}_4:\text{Cr}^{3+}$ ($x = 0 - 1$) solid solution was investigated. The processed data are plotted in Figure 3; data are not phase-corrected to be consistent with previous literature reports. Looking closely at the first coordination shell, the first near neighbor is the octahedrally coordinated Cr atom ($[\text{CrO}_6]$), located at ~ 1.5 Å. Next, between 2.0 Å and 3.5 Å, the second and third coordination shells can be assigned as the first cationic neighbor, Cr–Ga or Cr–Al ($\text{Cr}-[\text{Ga/AlO}_6] \approx 2.6$ Å) and the second cationic neighbor, Cr–Zn interactions ($\text{Cr}-[\text{ZnO}_4] \approx 3.5$ Å) respectively.^{47, 48, 54-56} When $x = 0$, there is an intense broad peak centered at ~ 2.6

Å, which is expected for $[\text{GaO}_6]$ and $[\text{ZnO}_4]$ polyhedra.^{32, 56} Increasing the aluminum concentration decreases this peak's intensity and causes a significant broadening by $x = 0.25$. This peak becomes noticeably asymmetric at $x = 0.50$. Further increasing Al^{3+} content to $x = 0.75$ shows the EXAFS peak becomes bimodal, which is an indication of two distinct coordination environments for the second and third coordination shells. Finally, by $x = 1$ there are two independent peaks centered at ~ 2.5 Å and ~ 3.0 Å.³² This change in the peak shape is attributed to the site mixing between Ga^{3+} and Al^{3+} ; the smaller ionic radius of Al^{3+} ($r_{6\text{-coord}} = 0.535$ Å) compared to Ga^{3+} ($r_{6\text{-coord}} = 0.620$ Å) leads to an observed shortening of the interatomic distance between Cr–Al.⁵⁷ Noting that because the ionic radius of Zn^{2+} ($r_{6\text{-coord}} = 0.600$ Å) is nearly the same as Ga^{3+} , the narrower, more intense peak observed in $x = 0$ is present.⁵⁷ Thus, with increasing concentration of the smaller Al^{3+} ion, the two shells (second and third) become more resolved because of the difference in ionic radii. This is consistent with the observations made in the XANES region with increasing width of peak D.

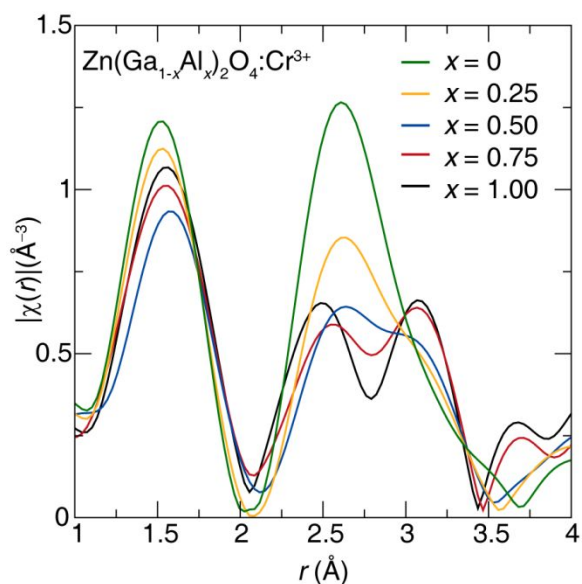


Figure 3. Real-space k^2 -weighted magnitude of the Cr K EXAFS across the solid solution $\text{Zn}(\text{Ga}_{1-x}\text{Al}_x)_2\text{O}_4:\text{Cr}^{3+}$ ($x = 0 - 1$) First coordination shell

([CrO₆]) at ~1.5 Å and the second ([Ga/AlO₆]) and third ([ZnO₄]) coordination shells ~2.5 Å and ~3.0 Å, respectively. Data are not phase corrected, to be consistent with previous literature reports.

To determine the interatomic distances of Cr–O, Cr–Ga/Al, and Cr–Zn, the EXAFS data were fit using the *IFEFFIT* software for the *r*-range (interatomic distance) of 1 Å to 4 Å using a Hanning window for the full range of *x*.⁴⁶ It is straight forward to model the data of the end members of the solid solution; however, modeling statistical atomic mixing using *IFEFFIT* is problematic because it is complicated to generate the complex scattering paths needed to describe these situations.⁴⁶ The intermediate values of *x* in this spinel-type structure, *i.e.*, *x* = 0.25, 0.50, and 0.75, all contain statistical mixing of the Ga/Al position (*B*-site). As a result, ordered models with a reduced *B*-site symmetry must first be created for use as starting structure models for *IFEFFIT*. These structural models can be constructed from DFT optimized crystal structures using the program “Supercell.”⁵⁸

A supercell approach is a classic method for approximating atomic disorder in a material by lowering the point symmetry and reducing Wyckoff multiplicity of each site. The result is a straightforward way to computationally mimic atomic disorder: enumerate and probe all possible combinations of local environments. Each of the ordered crystal structures generated is optimized, and DFT is used to determine the lowest (total) energy crystal structure, which is likely the best computational model for the experimentally observed mixing. For Zn(Ga_{1-*x*}Al_{*x*})₂O₄ (*x* = 0 – 1) the lowest total DFT calculated energies for each composition are visualized in Figure 4. In light of the fact that each model was calculated in the absence of Cr, a Cr atom was subsequently substituted into the structures in the Artemis software, and the Cr-containing structures were henceforth used to calculate the scattering paths in *IFEFFIT* as a starting point for fitting the EXAFS. Substitution of Cr onto

various Ga and Al sites in the FEFF calculations was attempted to determine the most reasonable model, and as a test to confirm if the chosen substitution would alter the average interatomic distances. It was found that the calculated interatomic distance between Cr–O, Cr–Ga/Al, and Cr–Zn were not dependent on where Cr was substituted. Therefore, the same crystallographic site for Cr was chosen across the full range of x in $\text{Zn}(\text{Ga}_{1-x}\text{Al}_x)_2\text{O}_4$ ($x = 0 - 1$). As the DFT model is only used as a starting point for the EXAFS fitting, the exact structure for the starting model is not critical.

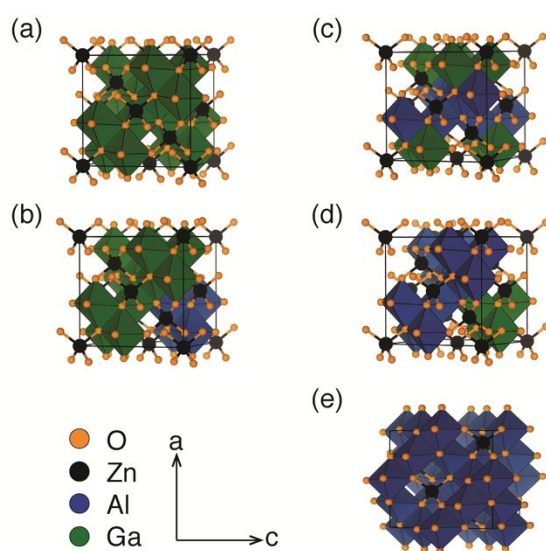


Figure 4. Unit cells of the solid-solution from DFT calculations $[\text{GaO}_6]$ (green) and $[\text{AlO}_6]$ (blue) octahedron are highlighted, Zn^{2+} (black), and O^{2-} (orange). (a) ZnGa_2O_4 (b) $\text{Zn}(\text{Ga}_{0.75}\text{Al}_{0.25})_2\text{O}_4$ (c) $\text{Zn}(\text{Ga}_{0.50}\text{Al}_{0.50})_2\text{O}_4$ (d) $\text{Zn}(\text{Ga}_{0.25}\text{Al}_{0.75})_2\text{O}_4$ and (e) ZnAl_2O_4 .

The final model fits the phase-corrected Cr K edge EXAFS across the full range of x are presented in Figure 5, as both the real-space k^2 -weighted magnitude (Figure 5a), as well as the real component (Figure 5b). The fits are in good agreement with the observed data, as well as a previous report on $\text{ZnGa}_2\text{O}_4:\text{Cr}^{3+}$ and $\text{ZnAl}_2\text{O}_4:\text{Cr}^{3+}$.³³ The fit parameters including the degeneracy of the absorbing atom (N), interatomic distance (r) of the atomic

neighbors, the difference between r_{DFT} (r in the DFT-optimized structure) and r (Δr), and the Debye-Waller factor (σ^2) are provided in Table S2. Notably, σ^2 , which measures the disorder in the path, is significant for the Cr–O path in $x = 0.50$ in support of disorder in the crystal structure, as predicted. The parameter N , as previously mentioned, is the degeneracy of the absorbing atoms. In other words, it is the number of atoms that are the same in the neighboring position to the absorbing atom, which in this case is Cr^{3+} (Table S3). So, when $N = 6$ for the first near neighbor of Cr^{3+} , there are six oxygen atoms as the first neighbor (e.g., a $[\text{CrO}_6]$ octahedron). For intermediate members of the solid solution, $\text{Zn}(\text{Ga}_{1-x}\text{Al}_x)_2\text{O}_4$ with values of $x = 0.25, 0.50,$ and 0.75 , the second shell of Cr (the first cationic neighbor), also has a total value of $N = 6$. Likewise, $N = 6$ for Cr–Zn interaction is also consistent with a $[\text{ZnO}_4]$ tetrahedron.⁵⁴

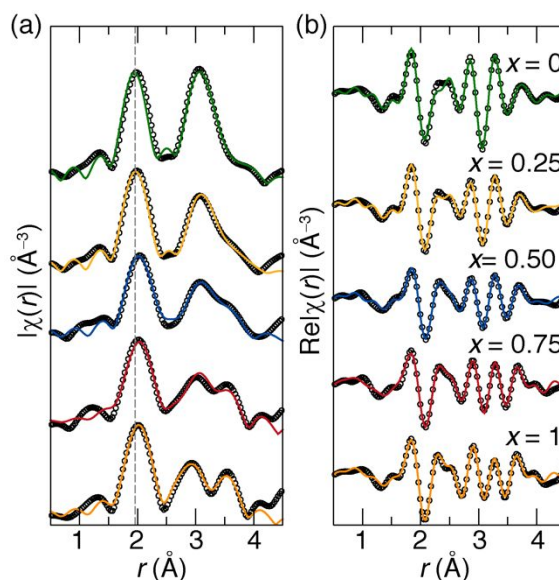


Figure 5. Phase-corrected real-space k^2 -weighted (a) magnitude and (b) real component of the Cr K edge EXAFS. Black circles are the observed data; the solid line is the fit. The dashed line is a guide for the eye to show the peak shift while the peak at ~ 3.2 Å splits with increasing x .

Examining the changes in the interatomic distance across the $\text{Zn}(\text{Ga}_{1-x}\text{Al}_x)_2\text{O}_4:\text{Cr}^{3+}$ ($x = 0 - 1$) solid solution for the first near neighbor revealed a particularly interesting change as a function of Al^{3+} content (x). A closer look at Figure 5a reveals that a shift to longer r with increasing Al^{3+} content is occurring for $x = 0.25$ and 0.50 . Once Al^{3+} content increases to $x = 0.75$, there is a small shift to a shorter value of r , and finally, another shift to smaller r when $x = 1$. This is consistent with a distortion in the polyhedron of Cr–O. Accordingly, a plot of r for the Cr–O bond (first near neighbor or $[\text{CrO}_6]$ octahedron) across the solid solution is shown in Figure 6. The difference between the interatomic distance of the DFT-calculated structure (r_{DFT}) and the interatomic distance determined by fitting the EXAFS (r) is indicated by Δr (Table S3).⁴⁷ Owing to the nature of the muffin-tin potentials used in EXAFS modeling, $|\Delta r|$ should not exceed 0.05 \AA to ensure there is no significant deviation from the initial model,⁴⁷ which is valid for all samples presented here when considering the Cr–O interactions. Larger deviations in the Cr–Al and Cr–Ga interatomic distances are present for intermediate members of the substitutional series, owing to the difference in ionic radii between octahedral Al^{3+} ($r_{6\text{-coord}} = 0.535 \text{ \AA}$) and Ga^{3+} ($r_{6\text{-coord}} = 0.620 \text{ \AA}$).⁵⁷ Although more significant deviations can sometimes lead to difficulties with the EXAFS modeling, the final interatomic distances determined by the EXAFS model here are consistent with the interatomic distances determined by Rietveld refinement of powder diffractograms from the same samples (Table S1).

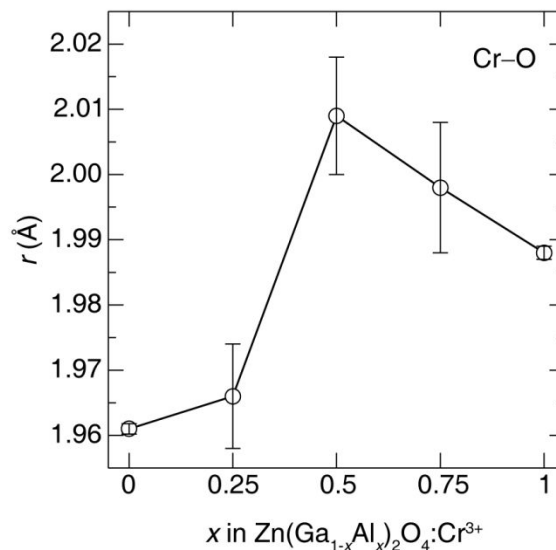


Figure 6. Interatomic distance (r) determined by fitting the Cr K EXAFS, of Cr–O as a function of x in Zn(Ga_{1-x}Al_x)₂O₄:Cr³⁺ ($x = 0 - 1$).

The models generated here by fitting the EXAFS suggest that as Al³⁺ increases to $x = 0.50$, there is an increase in the number of lattice defects. These defects are presumably Zn/Ga antisite defects, but the size and electron count of Zn²⁺ and Ga³⁺ are too similar to be modeled appropriately using X-ray diffraction or EXAFS, particularly given the level of inversion is estimated to be ~3% in the full gallate.^{31, 32} The Cr–O bond shows an increase in the r with increasing Al³⁺ up to $x = 0.50$ and then decreases for $x = 0.75$ and again when $x = 1$. This is in agreement with the thermoluminescence measurements of Zn(Ga_{1-x}Al_x)₂O₄:Cr³⁺ ($x = 0 - 1$) that revealed that as Al³⁺ content is increases from $x = 0$ to $x = 0.50$ the number of trap states increased, and that when Al³⁺ was further increased to $x = 0.75$ and 1 there were no trap states measured.²¹ Finally, it should be noted that ZnAl₂O₄:Cr³⁺ is reported to be a nearly normal spinel and does not have a visible long luminescent lifetime.^{21, 32} Taken together, introduction of Al³⁺ from $x = 0$ to $x = 0.50$ increases the defect concentration, the thermoluminescent lifetime, and distorts the [CrO₆]

octahedron and lengthens the average Cr–O bond length. Further introduction of Al³⁺ leads to a more idealized normal spinel, reducing the thermoluminescent lifetime and the Cr–O bond length.

3.3 EXAFS Spectra of Zn K Edge

Further evidence of local structure disorder around the Cr³⁺ luminescent center in the Zn(Ga_{1-x}Al_x)₂O₄:Cr³⁺ ($x = 0 - 1$) solid solution can be examined using the Zn–O interaction. A report of ZnGa₂O₄:Cr³⁺ that investigated the influence of varying the nominal concentrations of Zn/Ga where Zn was loaded either on stoichiometry, in excess, or in a deficiency, postulated an increase of defect concentration could be observed with increasing Zn content.³² Therefore, when Zn was in excess of Ga, this should result in the highest concentration of defects present in the structure.³² Moreover, these XAS experiments suggested a linear relationship between Zn–O bond length and defect concentration, such that, as bond length increased so would defect concentration.³²

X-ray absorption spectra were collected at the Zn K edge at 9659 eV to examine the EXAFS. The resulting data are plotted in Figure 7 and can be described in a similar manner as the Cr K edge data; data are not phase corrected, to be consistent with previous literature reports. Here, the first coordination shell is Zn–O interaction that represents the [ZnO₄] tetrahedra and is centered at ≈ 1.5 Å. The second peak located at ≈ 3.0 Å consists of the second and third coordination shells attributed to the Zn–Ga/Al ([Ga/AlO₆]) interaction and the Zn–Zn ([ZnO₄]) interaction.⁵⁹

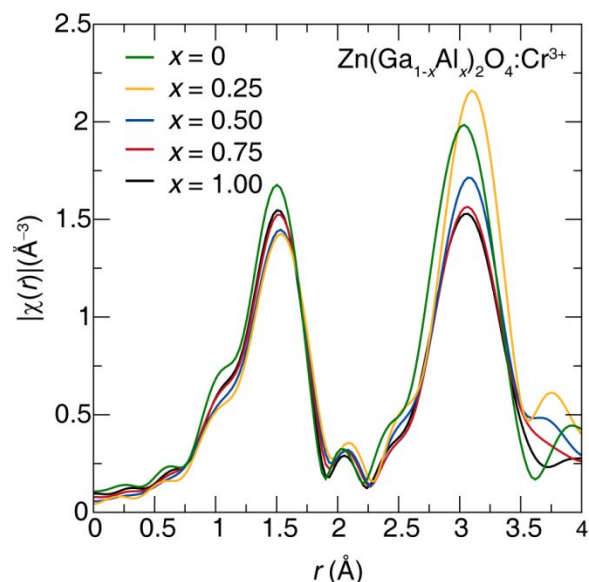


Figure 7. Real-space k^2 -weighted magnitude of the Zn K EXAFS across the solid solution $\text{Zn}(\text{Ga}_{1-x}\text{Al}_x)_2\text{O}_4:\text{Cr}^{3+}$ ($x = 0 - 1$). First coordination shell ([ZnO₄]) at ~ 1.5 Å and the second ([Ga/AlO₆]) and third ([ZnO₄]) coordination shell ~ 3.0 Å. Data are not phase corrected, to be consistent with previous literature reports.

The Zn K edge EXAFS for the full range of x in $\text{Zn}(\text{Ga}_{1-x}\text{Al}_x)_2\text{O}_4:\text{Cr}^{3+}$ ($x = 0 - 1$) was modeled and fit against the experimental data, using optimized DFT structures as a starting model. The calculated EXAFS closely reproduces the experimental data, as shown in the phase-corrected real-space k^2 -weighted of the magnitude (Figure 8a) and the real component (Figure 8b). The fitting parameters are listed in Table S4 in the supporting information, and the values of N for each coordination shell across the full solid solution are listed in Table S5. Looking closely at Figure 8a shows that as the Al^{3+} content increases, there is a slight shift to shorter values of r for the first coordination shell. Moreover, examining the second peak assigned to the second and third coordination environment, it can be seen that as Al^{3+} content increases to $x = 0.50$ the peak widens and then becomes narrow again when $x = 1$. This likely arises due to an increase in the number of lattice defects as Al^{3+} increases.

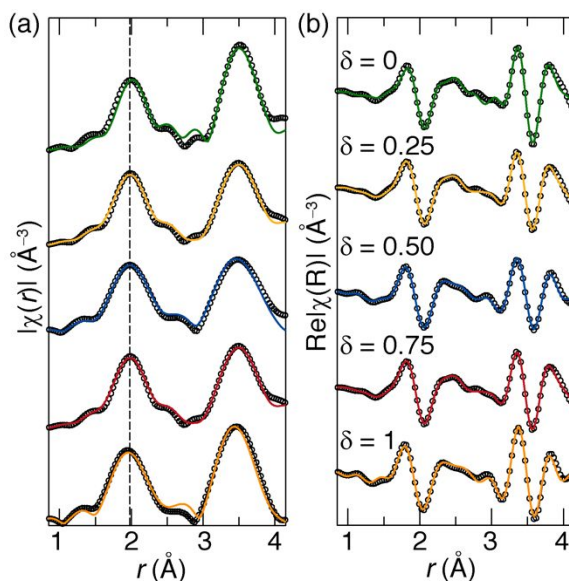


Figure 8. Phase-corrected real-space k^2 -weighted (a) magnitude and (b) real component of the Zn K edge EXAFS. Black circles are the observed data; the solid line is the fit. The dashed line is a guide for the eye to show the peak shift.

A closer examination of the fitting results is shown in Figure 9, where the Zn–O and Zn–Ga interactions are plotted as a function of x . The Zn–O interatomic distance decreases as a function of x linearly (Figure 9a) suggesting that there is no clear relationship with $[\text{ZnO}_4]$ tetrahedra and the presence of defects in this system. Conversely, the Zn–Ga interaction shows an increase in r up to $x = 0.50$ that is followed by a dramatic decrease in r when $x = 0.75$ (Figure 9b). The interatomic distances determined by EXAFS in this study are in good agreement with the interatomic distances from the previously reported Rietveld refinements (Table S1).²¹ Moreover, the trend in the Zn–Ga distance (Figure 9) is closely associated with the trend in Cr–O distance seen earlier (Figure 6).

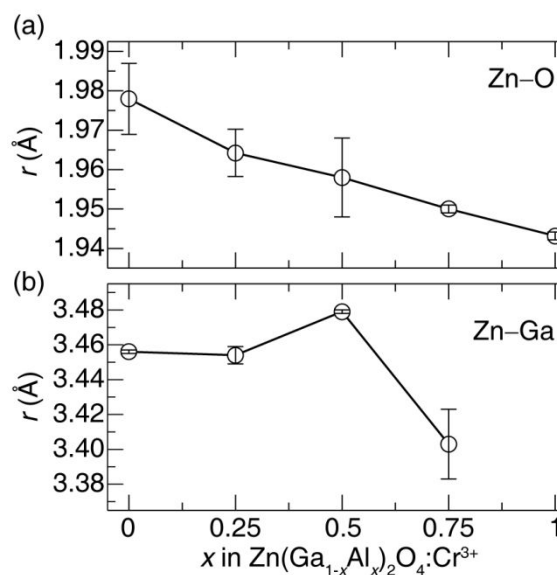


Figure 9. Interatomic distances determined by fitting the Zn K EXAFS. (a) Interatomic distance (r) of Zn–O as a function of x in $\text{Zn}(\text{Ga}_{1-x}\text{Al}_x)_2\text{O}_4:\text{Cr}^{3+}$ ($x = 0 - 1$). (b) Interatomic distance (r) of Zn–Ga as a function of x in $\text{Zn}(\text{Ga}_{1-x}\text{Al}_x)_2\text{O}_4:\text{Cr}^{3+}$ ($x = 0 - 1$).

To highlight the close correspondence between these relevant physical features, Figure 10 highlights the change in interatomic distances Cr–O and Zn–Ga together with the measured number of trap states from the previously reported thermoluminescence.²¹ Here, the difference in r is the change in interatomic distance from the stoichiometric ZnGaO_4 . With increasing Al content, x in $\text{Zn}(\text{Ga}_{1-x}\text{Al}_x)_2\text{O}_4:\text{Cr}^{3+}$ ($x = 0 - 1$), as x increases from $x = 0$ to $x = 0.50$ there is an increase in r that is closely correlated to an increase in the number of trap states; followed by a decrease in interatomic distance and a loss of trap states when $x = 0.75$. This relationship can then be inversely correlated to the reported long luminescent lifetimes where $x = 0$ is 6.0(2) min which decreases to 5.7(2) min at $x = 0.25$ and then decreases significantly to 2.4(2) min at $x = 0.50$ and is ultimately quenched

at $x = 0.75$.²¹ The data observed here supports that local structure distortions resulting from defects around the $[\text{GaO}_6]$ and $[\text{CrO}_6]$ octahedron are strongly correlated, and likely contributing, to changes in the persistent luminescence of the system.

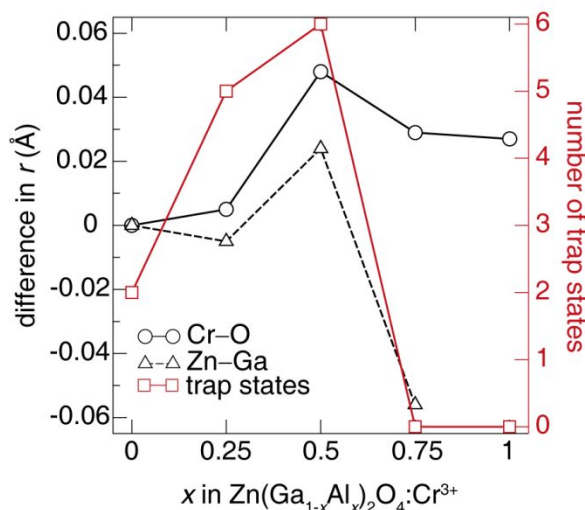


Figure 10. The difference in the interatomic distance (r) of Cr–O (circle) and Zn–Ga (triangle) compared to the number of trap states (red) measured from thermoluminescence as a function of composition. Local structure distortions resulting from defects around the $[\text{GaO}_6]$ and $[\text{CrO}_6]$ octahedron are strongly correlated, and likely contributing, to changes in the persistent luminescence of the system

4 Conclusion

In summary, this work provides extensive and direct evidence for the structure-defect-property relationship that has remained absent in understanding persistent luminescence phosphors. The XANES data collected on the $\text{Zn}(\text{Ga}_{1-x}\text{Al}_x)_2\text{O}_4:\text{Cr}^{3+}$ ($x = 0 - 1$) solid solution confirms the primary oxidation state of Cr in this system is 3+ and resides in an $[\text{CrO}_6]$ octahedron. Fitting these spectra reveals changes in peak shape that are consistent with

structural distortions in the $[\text{CrO}_6]$ octahedron, most likely arising from anti-site defects. Fitting the EXAFS indeed verifies the $[\text{CrO}_6]$ octahedral distortion along the C_3 axis is accompanied by an increase in the concentration of lattice defects as the Al^{3+} content increases from $x = 0 - 0.50$. Moreover, to substantiate the observed distortions observed in the Cr K edge the EXAFS, the Zn K edge was also examined. We show the decreasing Zn–O interatomic distances are proportional to the increase in Al^{3+} concentration. Conversely, the Zn–Ga interatomic distance increase up to $x = 0.50$ and then dramatically decrease when $x = 0.75$, which is correlated to the observations made in the Cr–O interaction. These results, combined with previously reported optical properties, support the hypothesis that lattice defects are an essential property to persistent luminescent phosphors and that a distortion in local coordination environments is sufficient to induce defects that influence the optical properties.

5 Acknowledgments

The authors (EF and JB) thank the National Science Foundation (DMR 18-47701) and the University of Houston Division of Research and the Grant to Enhance and Advance Research for funding this research. MWG thanks the Leverhulme Trust for funding via the Leverhulme Research Centre for Functional Materials Design. This research used the Maxwell/Opuntia/Sabine cluster(s) operated by the University of Houston and the Center for Advanced Computing and Data Systems (CACDS). Support for this work was also provided by resources of the uHPC cluster managed by the University of Houston and acquired through NSF Award Number 15-31814. XAS experiments were conducted under the use of the Advanced Photon Source, an Office of Science User Facility operated for the MRCAT operations are supported by the Department of Energy and the MRCAT member institutions. This research used resources of the Advanced Photon Source, a

U.S. Department of Energy (DOE) Office of Science User Facility operated for the DOE Office of Science by Argonne National Laboratory under Contract No. DE-AC02-06CH11357. The authors would also like to thank the staff scientists at MRCAT for assistance with sample preparation on site and assistance in collecting data. A special thank you to Blake Day for his help preparing the samples for XAS analysis, Kush Patel assistance with the DFT calculations, and Harvey for being the best therapy dog any research group could ask for.

6. References

1. J. Xu and S. Tanabe, *J. Lumin.*, 2018, **205**, 581-620.
2. W. M. Yen, S. Shinonoya and H. Yamamoto, *Phosphor Handbook*, CRC Press, Boca Raton, FL, 2007.
3. T. Maldiney, G. Sraiki, B. Viana, D. Gourier, C. Richard, D. Scherman, M. Bessodes, K. Van den Eeckhout, D. Poelman and P. F. Smet, *Opt. Mat. Express*, 2012, **2**, 261-268.
4. Q. le Masne de Chermont, C. Chanéac, J. Seguin, F. Pellé, S. Maîtrejean, J.-P. Jolivet, D. Gourier, M. Bessodes and D. Scherman, *Proc. Natl. Acad. Sci. U.S.A.*, 2007, **104**, 9266-9271.
5. A. Abd McKayum, J.-T. Chen, Q. Zhao and X.-P. Yan, *J. Am. Chem. Soc.*, 2013, **135**, 14125-14133.
6. A. S. Paterson, B. Raja, V. Mandadi, B. Townsend, M. Lee, A. Buell, B. Vu, J. Brgoch and R. C. Willson, *Lab Chip*, 2017, **17**, 1051-1059.
7. A. S. Paterson, B. Raja, G. Garvey, A. Kolhatkar, A. E. V. Hagström, K. Kourentzi, T. R. Lee and R. C. Willson, *Anal. Chem.*, 2014, **86**, 9481-9488.
8. K. Van den Eeckhout, P. F. Smet and D. Poelman, *Materials*, 2010, **3**, 2536.
9. K. Van den Eeckhout, D. Poelman and P. Smet, *Materials*, 2013, **6**, 2789.
10. P. F. Smet, J. Botterman, K. Van den Eeckhout, K. Korthout and D. Poelman, *Opt. Mater.*, 2014, **36**, 1913-1919.
11. J. Botterman, J. J. Joos and P. F. Smet, *Phys. Rev. B*, 2014, **90**, 085147.
12. T. Aitasalo, P. Dereń, J. Hölsä, H. Jungner, J. C. Krupa, M. Lastusaari, J. Legendziewicz, J. Niittykoski and W. Stręk, *J. Solid State Chem.*, **171**, 114-122.
13. F. Clabau, X. Rocquefelte, S. Jobic, P. Deniard, M. H. Whangbo, A. Garcia and T. Le Mercier, *Chem. Mater.*, 2005, **17**, 3904-3912.
14. P. Dorenbos, *J. Electrochem. Soc.*, 2005, **152**, H107-H110.
15. P. Dorenbos, *Phys. Status Solidi B*, 2005, **242**, 7-9.
16. Z. Yixi, U. Jumpei and T. Setsuhisa, *Appl. Phys. Express*, 2013, **6**, 052602.
17. K. Van den Eeckhout, P. F. Smet and D. Poelman, *Materials*, 2011, **4**, 980.
18. E. Finley, A. Mansouri Tehrani and J. Brgoch, *J. Phys. Chem. C*, 2018, **122**, 16309-16314.
19. B. Qu, B. Zhang, L. Wang, R. Zhou and X. C. Zeng, *Chem. Mater.*, 2015, **27**, 2195-2202.

20. A. De Vos, K. Lejaeghere, D. E. P. Vanpoucke, J. J. Joos, P. F. Smet and K. Hemelsoet, *Inorg. Chem.*, 2016, **55**, 2402-2412.
21. E. Finley and J. Brgoch, *J. Mater. Chem. C*, 2019, **7**, 2005-2013.
22. S. Carlson, J. Hölsä, T. Laamanen, M. Lastusaari, M. Malkamäki, J. Niittykoski and R. Valtonen, *Opt. Mater.*, 2009, **31**, 1877-1879.
23. K. Korthout, K. Van den Eeckhout, J. Botterman, S. Nikitenko, D. Poelman and P. F. Smet, *Phys. Rev. B*, 2011, **84**, 085140.
24. J. Hölsä, T. Aitasalo, H. Jungner, M. Lastusaari, J. Niittykoski and G. Spano, *J. Alloys Compd.*, 2004, **374**, 56-59.
25. M. Allix, S. Chenu, E. Véron, T. Poumeyrol, E. A. Kouadri-Boudjelthia, S. Alahraché, F. Porcher, D. Massiot and F. Fayon, *Chem. Mater.*, 2013, **25**, 1600-1606.
26. D. Gourier, A. Bessière, S. K. Sharma, L. Binet, B. Viana, N. Basavaraju and K. R. Priolkar, *J. Phys. Chem. Solids*, 2014, **75**, 826-837.
27. A. Bessière, S. K. Sharma, N. Basavaraju, K. R. Priolkar, L. Binet, B. Viana, A. J. J. Bos, T. Maldiney, C. Richard, D. Scherman and D. Gourier, *Chem. Mater.*, 2014, **26**, 1365-1373.
28. N. Basavaraju, K. R. Priolkar, A. Bessière, S. K. Sharma, D. Gourier, L. Binet, B. Viana and S. Emura, *Phys. Chem. Chem. Phys.*, 2017, **19**, 1369-1377.
29. Z. Yixi, U. Jumpei and S. Tanabe, *J. Mater. Chem. C*, 2013, **1**, 7849-7855.
30. A. Bessière, S. Jacquart, K. Priolkar, A. Lecointre, B. Viana and D. Gourier, *Opt. Express*, 2011, **19**, 10131-10137.
31. N. Basavaraju, S. Sharma, A. Bessière, B. Viana, D. Gourier and K. R. Priolkar, *J. Phys. D: Appl. Phys.*, 2013, **46**, 375401.
32. N. Basavaraju, K. R. Priolkar, D. Gourier, S. K. Sharma, A. Bessiere and B. Viana, *Phys. Chem. Chem. Phys.*, 2015, **17**, 1790-1799.
33. N. Basavaraju, K. R. Priolkar, D. Gourier, A. Bessiere and B. Viana, *Phys. Chem. Chem. Phys.*, 2015, **17**, 10993-10999.
34. R. M. Macfarlane, *J. Chem. Phys.*, 1963, **39**, 3118-3126.
35. H. M. Kahan and R. M. Macfarlane, *J. Chem. Phys.*, 1971, **54**, 5197-5205.
36. R. M. Macfarlane, *J. Chem. Phys.*, 1965, **42**, 442-442.
37. R. Chen and S. W. S. McKeever, *Theory of Thermoluminescence and Related Phenomena*, World Scientific, 1997.
38. J. K. Hornstra, E., *Philips Res. Rep.*, 1972, **27**, 76-81.
39. J. Hafner, *J. Comput. Chem.*, 2008, **29**, 2044-2078.
40. G. Kresse and D. Joubert, *Phys. Rev. B*, 1999, **59**, 1758.
41. G. Kresse and J. Furthmüller, *Phys. Rev. B*, 1996, **54**, 11169.
42. J. P. Perdew, K. Burke and M. Ernzerhof, *Phys. Rev. Lett.*, 1996, **77**, 3865-3868.
43. K. Momma and F. Izumi, *J. Appl. Crystallogr.*, 2011, **44**, 1272-1276.
44. C. U. Segre, N. E. Leyarowska, L. D. Chapman, W. M. Lavender, P. W. Plag, A. S. King, A. J. Kropf, B. A. Bunker, K. M. Kemner, P. Dutta, R. S. Duran and J. Kaduk, *AIP Conf. Proc.*, 2000, **521**, 419-422.
45. A. J. Kropf, J. Katsoudas, S. Chattopadhyay, T. Shibata, E. A. Lang, V. N. Zyryanov, B. Ravel, K. Mclvor, K. M. Kemner, K. G. Scheckel, S. R. Bare, J. Terry, S. D. Kelly, B. A. Bunker and C. U. Segre, *AIP Conf. Proc.*, 2010, **1234**, 299-302.
46. B. Ravel and M. Newville, *J. Synchrotron Radiat.*, 2005, **12**, 537-541.
47. S. Calvin, *EXAFS for Everyone*, CRC Press, Boca Raton, FL, 2013.

48. S. Calvin, E. E. Carpenter, B. Ravel, V. G. Harris and S. A. Morrison, *Phys. Rev. B*, 2002, **66**, 224405.
49. The Materials Research Collaborative Access Team, <http://mrcat.iit.edu/>, (accessed 2018, 2018).
50. M. Kaneko, S. Matsuno, T. Miki, M. Nakayama, H. Ikuta, Y. Uchimoto, M. Wakihara and K. Kawamura, *J. Phys. Chem. B*, 2003, **107**, 1727-1733.
51. L. A. Grunes, *Phys. Rev. B*, 1983, **27**, 2111-2131.
52. W. Zhang, J. Zhang, Z. Chen, T. Wang and S. Zheng, *J. Lumin.*, 2010, **130**, 1738-1743.
53. H. T. Dixit, N., Cottenier, S., Saniz, R., Lamoen, D., Partoens, B., Van Speybroek, B., Waroquier, M., *New J. Phys.*, 2011, **13**, 2-10.
54. V. G. Harris, N. C. Koon, C. M. Williams, Q. Zhang, M. Abe, J. P. Kirkland and D. A. McKeown, *IEEE Trans. Magn.*, 1995, **31**, 3473-3475.
55. C. N. Chinnasamy, A. Narayanasamy, N. Ponpandian, K. Chattopadhyay, K. Shinoda, B. Jeyadevan, K. Tohji, K. Nakatsuka, T. Furubayashi and I. Nakatani, *Phys. Rev. B*, 2001, **63**, 184108.
56. C. Wei, Z. Feng, G. G. Scherer, J. Barber, Y. Shao-Horn and Z. J. Xu, *Adv. Mater.*, 2017, **29**, 1606800.
57. R. D. Shannon, *Acta Cryst. A*, 1976, **32**, 751-767.
58. K. Okhotnikov, T. Charpentier and S. Cadars, *J. Cheminf.*, 2016, **8**, 1-15.
59. N. Pathak, P. S. Ghosh, S. Saxena, D. Dutta, A. K. Yadav, D. Bhattacharyya, S. N. Jha and R. M. Kadam, *Inorg. Chem.*, 2018, **57**, 3963-3982.

TOC

